UC Berkeley
UC Berkeley Previously Published Works

Title

Few-Unit-Cell MFI Zeolite Synthesized using a Simple Di-quaternary Ammonium Structure-Directing Agent

Permalink

Journal

ISSN

Authors

Lu, Peng
Ghosh, Supriya
de Mello, Matheus Dorneles
et al.

Publication Date

2021-08-23

DOI

Peer reviewed

Few-Unit-Cell MFI Zeolite Synthesized using a Simple Di-quaternary Ammonium Structure-Directing Agent

Peng Lu, Supriya Ghosh, Matheus Dorneles de Mello, Huda Sharbini Kamaluddin, Xinyu Li, Gaurav Kumar, Xuekui Duan, Milinda Abeykoon, J. Anibal Boscoboinik, Liang Qi, Heng Dai, Tianyi Luo, Shaeel Al-Thabaiti, Katabathini Narasimharao, Zaheer Khan, Jeffrey D. Rimer, Alexis T. Bell, Paul Dauenhauer, K. Andre Mkhoyan and Michael Tsapatsis*

Abstract: Synthesis of a pentasil-type zeolite with ultra-small few-unit-cell crystalline domains, which we call FDP (few-unit-cell crystalline domain pentasil), is reported. FDP is made using bis-1,5(tributyl ammonium) pentamethylene cations as structure directing agent (SDA). This di-quaternary ammonium SDA combines butyl ammonium, in place of the one commonly used for MFI synthesis, propyl ammonium, and a five-carbon nitrogen-connecting chain, in place of the six-carbon connecting chain SDAs that are known to fit well within the MFI pores. X-ray diffraction analysis and electron microscopy imaging of FDP indicate ca. 10 nm crystalline domains organized in hierarchical micro-/meso-porous aggregates exhibiting mesoscopic order with an aggregate particle size up to ca. 5 μm. Al and Sn can be incorporated into the FDP zeolite framework to produce active and selective methanol-to-hydrocarbon and glucose isomerization catalysts, respectively.

Introduction

Zeolites composed of one- to few-unit-cell domains,[1–4] exhibit distinct, and for some uses superior, catalytic and adsorption performance compared to conventional zeolites.[5–10] In this context, the quest for synthetic methods to minimize the size of crystalline zeolitic domains while accomplishing their arrangement to form hierarchical porous materials and thin film membranes persists.[11] Of particular importance is the synthesis of MFI with crystalline domains on the order of one to few unit cells (ca. 10 nm or less) due to anticipated uses in catalysis, adsorption and membranes.[5,12] Moreover, since MFI in its all-silica (zeosil) form has been studied extensively as a prototype for templated crystal growth,[13–15] the synthesis of MFI crystals as close as possible to their nucleation stage is of fundamental significance. Ryoo and co-workers, soon after their discovery of gemini-type oligo-quaternary ammonium surfactants as organic structure-directing agents (SDAs) leading to multilamellar 2-dimensional MFI,[3] they reported the synthesis of mesoporous materials with walls composed of few-unit-cell domains with the zeolite beta (BEA) and MFI-like framework topologies.[16,17] We have shown that simpler short chain mono- and di-quaternary SDAs (i.e., without the dual porogenic ability of tri- to penta-quaternary ammonium gemini-surfactant SDAs with C18 alkyl chains) are also capable of directing

[*] Dr. P. Lu, Dr. T. Luo, Prof. M. Tsapatsis
Department of Chemical and Biomolecular Engineering &
Institute for NanoBioTechnology, Johns Hopkins University
3400 N. Charles Street, Baltimore, MD 21218 (USA)
E-Mail: tsapatsis@jhu.edu

S. Ghosh, X. Li, G. Kumar, X. Duan, Prof. P. Dauenhauer,
Prof. K. A. Mkhoyan
Department of Chemical Engineering and Materials Science
University of Minnesota
421 Washington Avenue SE, Minneapolis, MN 55455 (USA)

Dr. M. Dorneles de Mello, Dr. J. A. Boscoboinik
Catalysis Center for Energy Innovation, University of Delaware
Newark, DE 19716 (USA)
and
Center for Functional Nanomaterials
Brookhaven National Laboratory, Upton, NY 11973 (USA)

Dr. H. S. Kamaluddin, Prof. S. Al-Thabaiti, Prof. K. Narasimharao,
Prof. Z. Khan
Department of Chemistry, Faculty of Science
King Abdulaziz University, Jeddah 21589 (Saudi Arabia)

Dr. M. Abeykoon
National Synchrotron Light Source II
Brookhaven National Laboratory, Upton, NY 11973 (USA)

Dr. J. A. Boscoboinik
Department of Materials Science and Chemical Engineering, State
University of New York at Stony Brook
100 Nicolls Rd, Stony Brook, NY 11794 (USA)

Dr. L. Qi, Prof. A. T. Bell
Chemical Sciences Division, Lawrence Berkeley National Laboratory
Berkeley, CA 94720 (USA)
and
Department of Chemical and Biomolecular Engineering
University of California, Berkeley, CA 94720 (USA)

H. Dai, Prof. J. D. Rimer
Department of Chemical and Biomolecular Engineering
University of Houston, Houston, TX 77204 (USA)

Prof. M. Tsapatsis
Applied Physics Laboratory, Johns Hopkins University
11100 Johns Hopkins Road, Laurel, MD 20723 (USA)

the growth of single- to few-unit-cell thick nanosheets by hindering growth along the b-axis of MFI.[4,11] However, the use of such simple SDAs to reduce crystalline domains down to few unit cells in directions other than the MFI b-axis has not yet been achieved. Here, we demonstrate that few-unit-cell MFI, with a highly broadened XRD pattern, can be synthesized using a relatively simple di-quaternary ammonium (bis-1,5(tributyl ammonium) pentamethylene) cation (called here tri-Bu-dC5) as an SDA. All-silica, aluminosilicate, and stannosilicate MFI synthesis is reported along with sorption and catalytic properties.

Synthesis of MFI and MEL with different crystal habit, stacking fault sequence and presence of rotational intergrowths has been studied extensively.[18–20] We have demonstrated that at early stages of crystal growth (i.e., before crystal facets develop) bis-1,5(tripropyl ammonium) pentamethylene cations (called here tri-Pr-dC5) hinder all growth rates compared to those observed using tetrapropyl ammonium (TPA), the typical SDA for MFI synthesis. Moreover, we have shown that at early stages of growth, tri-Pr-dC5 favors growth along the b-axis compared to the other crystallographic directions of MFI, while stacking faults and rotational intergrowths attributable to the presence of MEL are not observed.[11,19] This finding combined with the well-established trends in MFI synthesis using its most common SDA, TPA cations, which favor growth along the c- and a-axes, lead us to hypothesize that at early stages of crystal growth (i.e., before well-developed crystal facets emerge) the pentamethylene moiety is responsible for reversing the crystal shape of MFI from thin to long platelets along its b-axis. The hypothesis that the pentamethylene moiety is responsible for favoring growth along the b-axis, is further corroborated by the finding that MFI growth using bis-1,6(tripropyl ammonium) hexamethylene cations (tri-Pr-dC6) retains the b-axis as a slower growing direction. We have also demonstrated that when using tetrabutyl ammonium (TBA) or phosphonium (TBP) SDAs, growth along the b-axis is hindered while MEL presence and rotational intergrowths are enhanced leading to single-unit-cell thick intergrown MFI nanosheets, a material we call SPP (self-pillared pentasil).[4] Scheme 1 illustrates these hypothesized opposing trends coded on bis-1,5(tributyl ammonium) pentamethylene cations (tri-Bu-dC5). Specifically, the favoring and hindering of (i) growth along the b-axis, (ii) MEL stacking faults, and (iii) rotational intergrowths by different parts of the molecule.

We decided to test the hypothesis that these opposing trends will create frustration in the SDA characteristics hindering crystal growth in all directions and limiting the resulting crystal size to few-unit-cells. An earlier attempt to the crystallization of MFI using this SDA was inconclusive as it did not yield crystalline material,[21] but
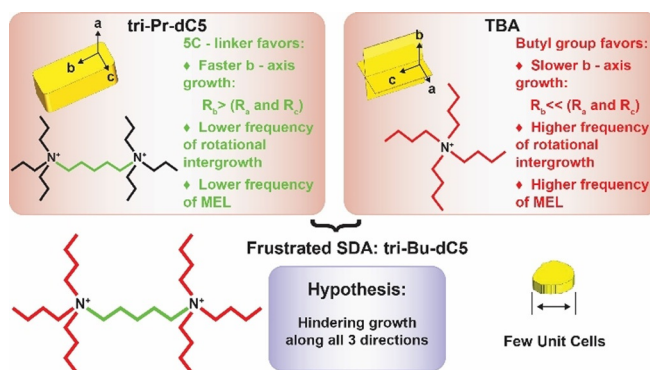
Scheme 1. Hypothesized opposing trends of tri-Bu-dC5 for minimizing growth along all directions to generate ultra-small crystallites. Black, green and red colors denote propyl, five methylene chain, and butyl groups, respectively.

confirmed our anticipation that the frustrated tri-Bu-dC5 SDA will not be a very effective SDA for MFI or MEL. Below, it is shown that it is possible to grow highly crystalline few-unit-cell pentasil zeolite, which we call FDP (few-unit-cell crystalline domain pentasil zeolite).

Results and Discussion

Characterization of the tri-Bu-dC5 SDA and its synthesis procedure are provided in the Supporting Information. The SDA was used in hydroxide form (tri-Bu-dC5(OH)$_2$) obtained by anion exchange of its bromide form (tri-Bu-dC5(Br)$_2$). The synthesis parameters along with crystal size and composition of the FDP zeolites synthesized at 120°C are summarized in Table 1. We note here that conventional MFI was obtained at the higher synthesis temperature of 150°C (Figure S2). The SDA exhibits structure-directing role towards MFI and was found to be preserved intact in the as-made product (Figure S3).

The wide angle XRD pattern of the calcined Si-FDP (1) zeolite (see Table 1 for sample denotation) shows two

Table 1: Summary of synthesis parameters and compositions of calcined FDP zeolites obtained at 120°C.

Material	Sol composition		Crystallite size [nm][a]	Si/Al or Si/Sn[b]	t [days]	Rotation or not
	H$_2$O/SiO$_2$	SDA/SiO$_2$				
Si-FDP (1)	38	0.15	6.0	–	7	yes
Si-FDP (2)	38	0.25	5.3	–	9	yes
Si-FDP (3)	13	0.15	7.3	–	3	yes
Si-FDP (4)	13	0.25	5.2	–	7	yes
Si-FDP (5)	8	0.15	4.0	–	3	yes
Al-FDP (1)	8	0.15	6.6	157 (100)	3	yes
Al-FDP (2)	8	0.15	7.5	172 (200)	3	yes
Al-FDP (3)	8	0.15	7.1	260 (300)	3	yes
Al-FDP (4)	8	0.15	7.7	42 (50)	3	yes
Al-FDP (5)	8	0.15	7.6	49 (50)	5	yes
Sn-FDP	8	0.15	8.0	105 (100)	7	no

[a] Calculated by Scherrer equation. [b] Obtained by ICP analysis; the numbers in parentheses indicate the molar ratio in the synthesis sol.
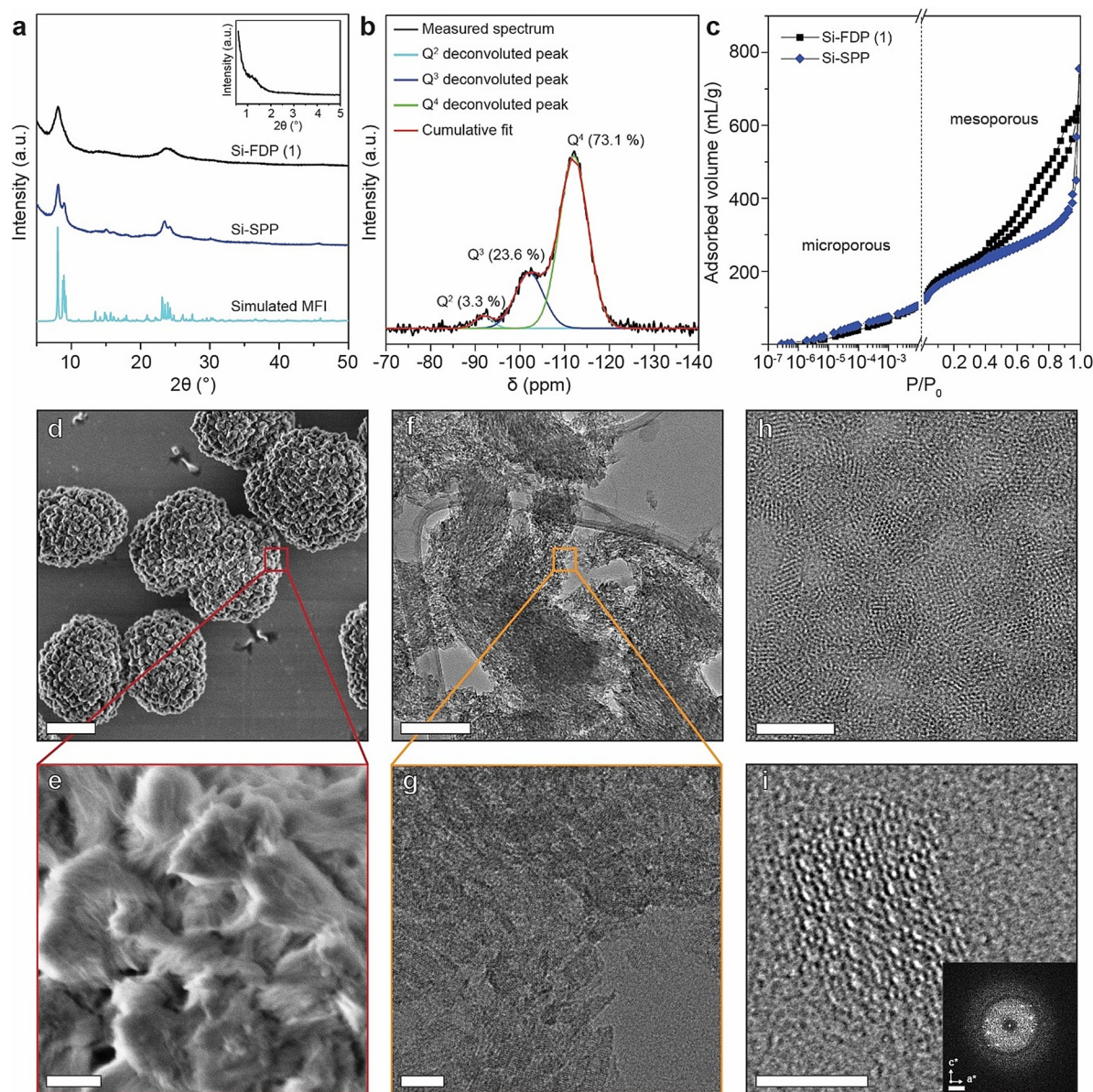
Figure 1. Characterization of Si-FDP (1). a) XRD patterns of (from top to bottom) calcined Si-FDP (1) zeolite, pure silica SPP zeolite synthesized using TBPOH and simulated MFI from the International Zeolite Association.[22] b) Solid-state ^{29}Si NMR spectra of Si-FDP (1). c) Ar adsorption/desorption isotherms of Si-FDP (1) and Si-SPP zeolites. d),e) Low and high magnification SEM images of the calcined Si-FDP (1) zeolite. f and g) Medium magnification TEM images of calcined Si-FDP (1). h) Higher magnification image showing nanoparticle clusters. i) Wiener-filtered HRTEM of individual MFI-nanoparticle oriented along the b-direction. Inset FFT is consistent with typical MFI spot pattern along b-axis. Scale bars: d) 2 µm; e) 200 nm; f) 200 nm; g) 20 nm; h) 20 nm, i) 5 nm, (i, inset FFT) 1 nm^{-1}.

resolved Bragg reflection peaks at $d = 1.09$ and 0.38 nm, consistent with the MFI framework type, though broadened (Figure 1 a, black trace). The XRD patterns of pure-silica SPP zeolite and simulated MFI framework are provided for comparison (Figure 1, blue and cyan traces). Low angle XRD (Figure 1 a, inset) of the calcined pure silica FDP zeolite showed a broad diffraction peak at around 1.3° 2θ, which could be ascribed to a prevalent regular distance between crystalline domains creating a short-range mesoscopic ordering. We notice that this mesoscopic order is created in the absence of gemini surfactant SDAs, which are known to template ordered mesoporosity,[17,23,24] Most likely, it is the

outcome of interrupted crystal growth and/or aggregation of few-unit-cell crystalline domains rather than templating by the SDA. To our knowledge, this is the first time that a mesostructured array of MFI nanocrystals is created using a simple SDA. Pair distribution function (PDF) analysis was performed to further assess the local structure of the FDP zeolites. The results demonstrated consistency of Si-FDP with the MFI structure, exhibiting similarity with the PDF of Si-SPP while deviating from defect-free F-MFI (MFI zeolite synthesized in fluoride medium) (Figure S4). The presence of the characteristic absorbance band at 550 cm^{-1} in FTIR spectra (Figure S5) further confirmed that Si-FDP is consis-

tent with the MFI topology. Also, the band at 950 cm^{-1}, an indicator of structural defects in zeolitic materials,[25] was observed in FDP zeolite and absent in F-MFI.

Three Si species were detected by solid-state ^{29}Si magic angle spinning (MAS) NMR for the pure silica FDP zeolite (Figure 1b). As expected, silanol groups were detected, as indicated by the resonance signal of Q^2 and Q^3 species, which in total comprise 26.9% of the Si species, a larger fraction than that of the single unit cell thick Si-SPP zeolite (ca. 23%) reported previously.[26] These silanol groups can be mostly attributed to the surface termination of the small crystalline domains in the FDP zeolites. Ar adsorption and desorption isotherms are shown in Figure 1c, where the sorption data of the pure silica SPP zeolite is also provided for comparison (the textural properties are summarized in Table S1). The isotherms show that Si-FDP zeolite, possesses both micro- and mesoporosity. The pore size distribution drawn up to 10 nm indicates micropores centered at 0.525 nm and meso-pores with a broad distribution from 2–7 nm (Figure S6a), which are comparable to that of SPP zeolite. The pore size distribution of SPP and FDP zeolites are very similar in the microporous region, but the latter exhibit larger mesopore volumes (Figure S6b).[26]

Low and high magnification SEM images (Figure 1, d and e) show large spherical particles comprised of smaller filamentous particles (ca. 200 nm), which are further comprised of much smaller crystallites (Figure 1, f and g). The HRTEM image is consistent with the particles comprised of nanocrystalline domains that are not crystallographically aligned (Figure 1h). An individual MFI nanoparticle with a size of ca. 5 nm oriented along its b-axis is shown in Figure 1i. Synthesis with higher SDA content (Si-FDP (2) with SDA/SiO$_2$ = 0.25) also yields porous aggregates comprised of similarly sized nano-crystallites (see Figures S7 and S8). The mean sizes of the crystalline domains calculated from XRD peak broadening (Table 1) are in good agreement with the anticipated values from inspecting the HRTEM images. Similar XRD broadening has been reported by Ryoo et al.,[3,17] when they synthesized hexagonally ordered meso-porous molecular sieves with MFI-like microporous walls and disordered MFI-like nanolayers interconnected in a disordered manner. A distinguishing characteristic of the current approach is that a simpler SDA is used and the ordered mesostructure is not templated by a long tail of the SDA.

When the H$_2$O/SiO$_2$ ratio was decreased from 38 to 13 and below, crystalline FDP zeolites could be obtained faster (Table 1). The wide angle XRD patterns of the calcined Si-FDP zeolites synthesized under low H$_2$O/SiO$_2$ ratio are similar to those of high H$_2$O/SiO$_2$ ratio (Figure S9, a and b). The aggregate particle size decreased with decreased water content, and its morphology changed from spheres of diameter ca. 3–5 μm (Figure 1d and Figures S7a and S8a) to filamentous aggregates of size ca.100–200 nm (Figure 2 and Figure S9). Unlike SPP zeolite particles that consist of orthogonally intergrown 2D nanosheets with single-unit-cell thickness, the FDP zeolite particles obtained at low water content display no orthogonal intergrowths. Ar adsorption and desorption isotherms and pore size distribution analysis (Figure S6) of Si-FDP (3) synthesized using a low H$_2$O/SiO$_2$
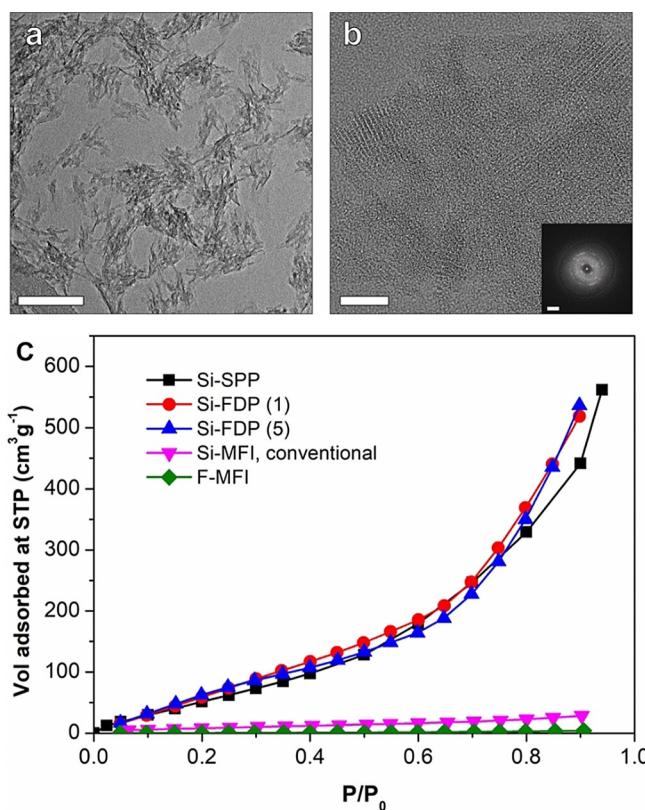
Figure 2. Low magnification (a) and high resolution (b) TEM images of Si-FDP (5) zeolite synthesized under low water content. Scale bar in (a) is 100 nm, and in (b) is 10 nm, (b, inset FFT) 2 nm^{-1}. c) Water vapor adsorption at 25°C for pure silica zeolites: Si-SPP (black square), Si-FDP (1) (red circle), Si-FDP (2) (blue triangle), conventional Si-MFI (pink inverted triangle), and F-MFI (green diamond).

ratio are similar to its high H$_2$O/SiO$_2$ counterpart. Si-FDP zeolite is stable at 550°C, while it gradually loses crystallinity at higher temperatures (Figure S10).

Water vapor adsorption isotherms on Si-FDP zeolites are shown in Figure 2c. Si-SPP, conventional Si-MFI and F-MFI are provided for comparison. Water sorption on Si-SPP and Si-FDP zeolites can be attributed to the presence of silanol groups on the external surfaces and the presence of meso-pores between the crystalline domains. In contrast, as anticipated, much lower water adsorption is observed on commercial Si-MFI and even lower on F-MFI in the entire pressure range.

To introduce sites for catalytic reactions, Al was incorporated into the FDP zeolite framework, as corroborated by the solid-state ^{27}Al magic angle spinning (MAS) NMR (Figure S11a) and well dispersed as shown by the EDX mapping (Figure S12). For Al-FDP (2) with lower Al content, a small fraction of extra-framework Al was detected (ca. 1.7% by peak area integration). Higher Al-containing FDP zeolites (Al-FDP (4) and Al-FDP (5)) show increased amounts of extra-framework Al, 18.4% and 12.1%, respectively (Figure S11a). Solid-state ^{29}Si magic angle spinning (MAS) NMR spectra (Figure S11b) for the Al-FDP zeolites show that the percentages of Q^2 and Q^3 species for Al-FDP (2), Al-FDP (4) and Al-FDP (5) (21.1%, 24.4% and 20.6%, respectively) are

reduced compared to those present in Si-FDP (1) (26.9%). To determine the above cited percentages, the deconvolution of the spectra was performed assuming that framework Al is only present as $Si(OSi)_3(OAl)$ species (i.e., neglects AlO-SiOH-containing species).[27,28] The resonance at ca. -107 ppm was assigned to $Si(OSi)_3OAl$ while the others were assigned to $Si(OSi)_2(OH)_2$ (ca. -91 ppm), $Si(OSi)_3(OH)$ (ca. -102 ppm), and $Si(OSi)_4$ (ca. -112 ppm and -115 ppm). It was previously reported that Al incorporation can lead to a decrease of the structural defects in zeolites synthesized in hydroxide medium.[29] The XRD patterns (Figure S11c) show better resolved shoulder peaks for the aluminosilicate FDP zeolites and the corresponding crystalline domain sizes calculated by the Scherrer equation are generally larger than those of the Si-FDP zeolites (Table 1). The Al incorporation did not change the morphology of the FDP zeolites, as shown by TEM images (Figure S13, a and c). Argon adsorption and desorption isotherms and pore size distribution analysis (Figure S6) of the Al-FDP zeolite presented higher mesopore volume than that of the Si-FDP zeolite. IR spectrum (Figure S14) of H-form Al-FDP (4) using pyridine as a probe shows absorption bands at 1455 cm^{-1} that can be ascribed to Lewis acid sites from extra-framework Al, and at 1545 cm^{-1} that can be assigned to Brønsted acid sites (BAS). Brønsted acidic properties of Al-FDP zeolites were characterized using in situ titrations with pyridine and 2,6-di-tertbutylpyridine (DTBP) during ethanol dehydration (see Supporting Information for details) and the results are shown in Table 2. Higher initial rate of diethyl ether (DEE) formation was observed on the higher Al containing FDP (Al-FDP (4)), which showed comparable turnover frequency (TOF) compared to its lower Al containing counterpart (Al-FDP (3)). The external BAS fraction reached as high as 73.2% for Al-FDP (4), which is much higher than that for Al-SPP (51%).[26]

Sn was also incorporated into the FDP framework as supported by the UV/Vis spectrum (Figure S15a), ^{119}Sn MAS NMR spectra (Figure S15b) and TEM imaging. The XRD patterns (Figure S16) show better resolved shoulder peaks of Sn-FDP zeolite than that of Si-FDP. The domain size of Sn-FDP zeolite calculated using the Scherrer equation is larger than those of the Si-FDP zeolites (Table 1). TEM images (Figure S13, b and d) show that Sn-FDP particles are composed of globular crystallites of few-unit-cell domains. Additional experiments with spatially resolved energy dispersive X-ray (EDX) analysis in scanning transmission electron microscopy (STEM) showed that Sn is presented and uniformly distributed in the Sn-FDP particles (Figure S17 and Figure 3a). High angle annular dark field (HAADF) STEM was used to examine the Sn distribution at higher resolution, confirming that Sn was incorporated in the framework and distributed evenly (Figure 3b) as no contrast attributable to Sn clusters can be observed except in very few images. The Si/Sn ratio in the product (105) is close to that of the starting synthesis sol (100) (Table 1).

The crystallization kinetics of FDP zeolites were investigated by monitoring the products collected at different crystallization times. Figure 4 shows the low and high magnification TEM images of as-made Si-FDP zeolites and the corresponding XRD patterns and crystallization curves are shown in Figure S18. No solid product could be collected up to 12 h heating, but small particles of ca. 15 nm were observed by TEM images (Figure 4a). HRTEM and corresponding FFT confirm that the particles are MFI-type (Figure 4, b and inset). No particles could be observed for the sol collected at 6 h. The powder collected at 18 h exhibits typical XRD pattern of FDP zeolite and high relative crystallinity of 90%, despite the very low relative yield of 3.3% (Figure S18, a and b). TEM imaging of the powder collected at 18 h shows polycrystalline particles with average size of ca. 42 nm (Figure 4, c and d). Prolonged heating to 24 h and above did not result in substantial changes of the crystallinity, but the yield gradually increased (Figure S18, a and b). Moreover, the particle size increased to ca. 69 nm, 112 nm and 180 nm for 24 h, 30 h and 48 h crystallization, respectively (Figure 4, e to j; Figure S19). Si-FDP without EtOH, Al-FDP and Sn-FDP show different nucleation and growth behaviors. The induction time (the period when no solid could be collected) was ca. 6 h, 6 h and 48 h for Si-FDP without EtOH, Al-FDP and Sn-FDP, respectively. EtOH and related alcohols could slow down crystallization as reported in a previous work.[30] For Si-FDP, 24 h heating rendered almost fully crystalline products (Figure S18, a to d), while it took longer for Al-FDP and Sn-FDP, (Figure S18, e to h).

Methanol-to-hydrocarbon (MTH) reactions were performed over the Al-FDP (5) zeolite and comparisons were made with SPP and commercial MFI (C-MFI) zeolites. Three different temperatures were tested, and it was found that there was a temperature threshold

Table 2: Catalytic characterization results of Al-FDP zeolites in ethanol dehydration.

Material	Initial rate of DEE formation [µmol g^{-1} min^{-1}][a]	TOF of DEE formation [mol mol H$^+_{Py}$$^{-1}$ h^{-1}][b]	Total BAS count [µmol g^{-1}][c]	Fraction of external sites [%][d]
Al-FDP (3)	1.23	1.7 ± 0.1	44	41 ± 6
Al-FDP (4)	1.93	1.1 ± 0.1	101	73 ± 3

[a] Reaction conditions: $T = 144 \pm 1\,°C$, $p_{EtOH} = 5.2$ torr, WHSV in the range 1.1–3.9 g EtOH/g cat./h, diluent flow rate 60 sccm. Only DEE was produced under the investigated conditions and no other products were detected. [b] TOF was calculated from the slope of the trace obtained while plotting mass-normalized rates [µmol g^{-1} h^{-1}] under pyridine (EtOH:pyridine ca. 503) as a function of the cumulative uptake of pyridine [µmol g^{-1}] and errors represent standard errors in slope estimation. [c] Total BAS counts were calculated from the cumulative pyridine uptakes for complete rate quenching assuming a stoichiometry of 1:1. [d] Fraction of external sites was calculated using DTBP titration (EtOH:DTBP ≈ 808) using two methods, namely (i) $f_{ext} = 1 -$ (rate after DTBP saturation/rate prior to DTBP introduction), and (ii) f_{ext} = cumulative uptake of DTBP/ cumulative uptake of pyridine, and the errors represent 95% confidence interval on the values obtained from the two methods for a single experimental run.
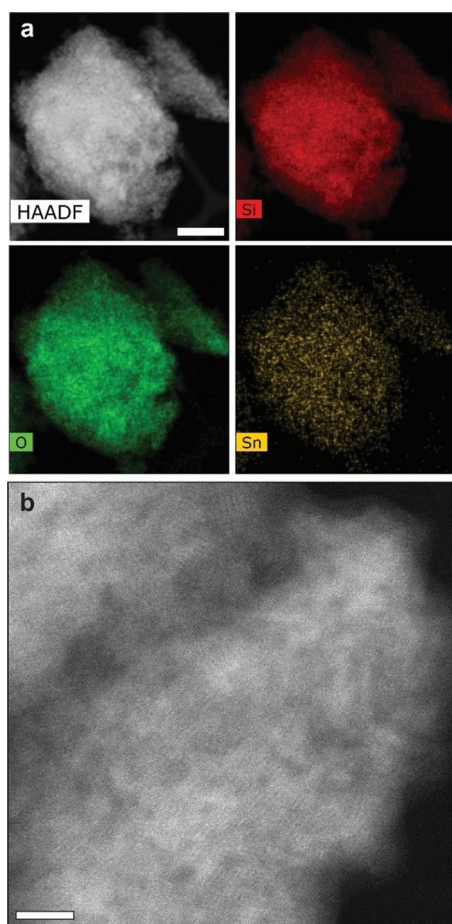
Figure 3. a) STEM-EDX elemental maps along with corresponding HAADF-STEM image and b) HAADF-STEM image of another particle showing uniform contrast from Sn-FDP with Si/Sn atomic ratio of 105. Scale bars: a) 500 nm; and b) 10 nm. These experiments were performed on aberration-corrected FEI Titan G2 60–300 STEM.[31]

for initiating the reaction for FDP zeolite. As shown in Figure 5a, only dimethyl ether (DME) was produced at 350 °C for FDP zeolite, while SPP and C-MFI demonstrated much higher activity to form hydrocarbons. When the temperature increased to 400 °C and then to 450 °C, considerable DME can still be detected in FDP zeolite, but it is hardly detectable for SPP and C-MFI zeolites. Methanol conversion increased along with the elevated temperature for the three catalysts, but FDP showed slightly lower conversion (95.7 % at 450 °C). A plausible reason for the existence of the temperature threshold to initiate MTH reaction could be due to the predominant BAS external acid fraction for FDP zeolite (>70 %, see Table 2). Moreover, at external sites, hydrocarbon pool species accumulation may be hindered favoring the olefin-based cycle exhibiting higher ratio of propylene to ethylene.[32–35] Indeed, FDP zeolite exhibited higher P/E (propylene to ethylene) ratio than SPP and C-MFI, e.g., 11.3 versus 4.7 and 5.6 at 450 °C. However, we note here that earlier studies demonstrated that different P/E ratios can be obtained using SPP zeolites when assessed under different reaction conditions, e.g., time-on-stream (TOS).[32–35] Therefore, proper attribution of the higher P/E ratio for FDP requires further studies.

Isomerization of glucose (GLU) to fructose (FRU) over the Sn-FDP zeolite was carried out as a probe reaction, following the procedures reported previously.[36] Sn-FDP zeolite achieved a FRU yield of 60 % at 96 % GLU conversion (Figure 5b, black solid square). This performance is comparable to that of Sn-SPP zeolite (Figure 5b, gray solid circle), where the high activity and selectivity was ascribed to the synergistic effect of Brønsted and Lewis acid sites along with the easy access to those active sites. Considering the similar framework topology and morphology resemblance between Sn-FDP and Sn-SPP zeolites, the proposed mechanism for Sn-SPP should also be applicable here. For the recyclability of the catalyst, we performed 3 consecutive reaction-regeneration cycles (see details in Supporting In-
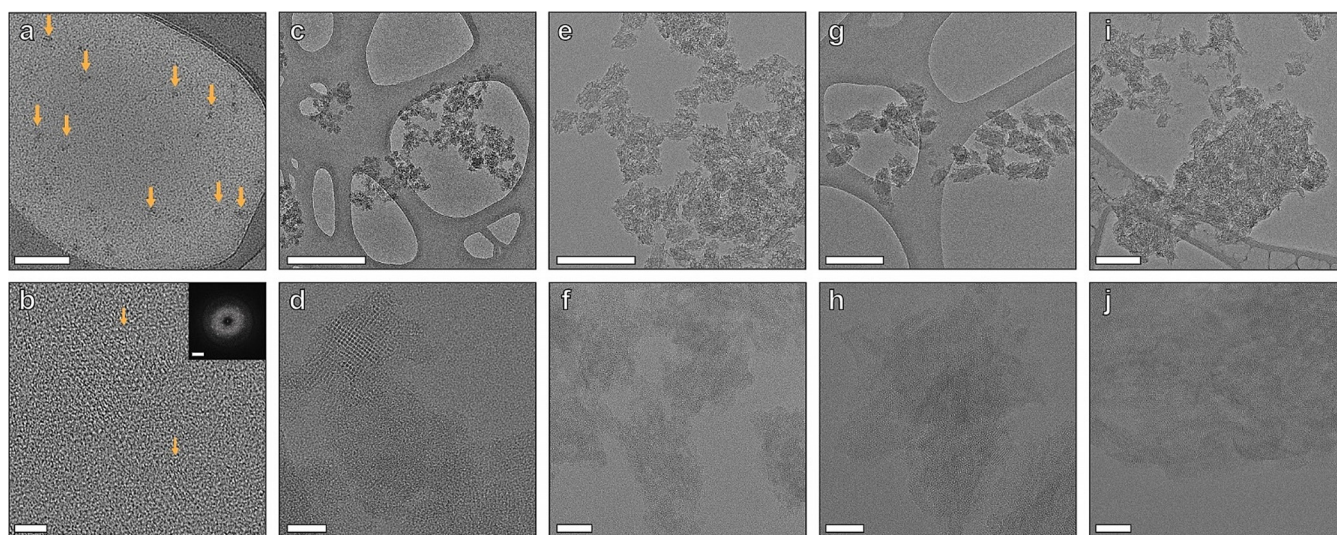

Figure 4. Low and high magnification TEM images of as-made Si-FDP zeolites collected from different crystallization times: a, b) 12 h; c, d) 18 h; e, f) 24 h; g, h) 30 h and i, j) 48 h. The synthesis sol composition is 1SiO$_2$:0.15 tri-Bu-dC5(OH)$_2$:13 H$_2$O:4 EtOH. Scale bars are: a) 100 nm; b) 5 nm, FFT 2 nm^{-1}; c, e, g, i,) 200 nm; d) 10 nm; f, h, j) 20 nm. Synthesis performed at 120 °C with a rotating autoclave.
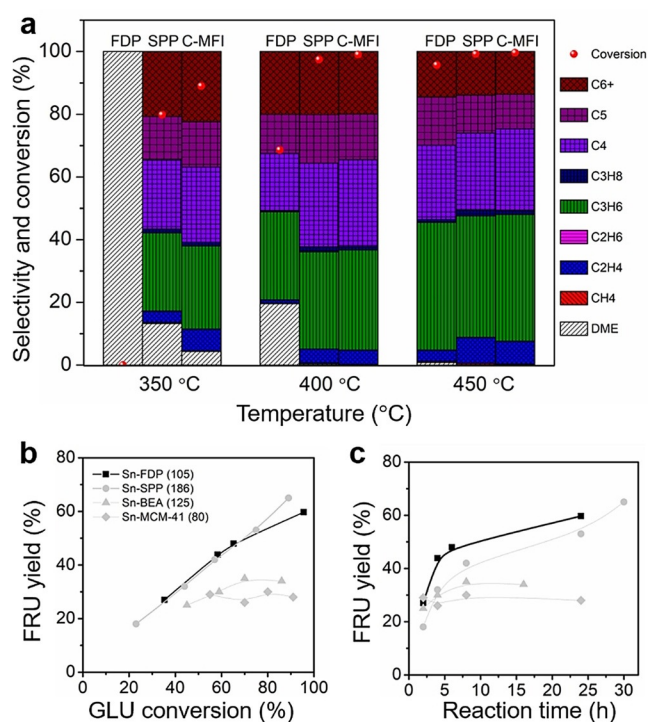
Figure 5. Catalytic evaluation of the FDP zeolite catalysts. (a) MTH reaction over Al-containing catalysts: Al-FDP (5), SPP (Si/Al: 36), and C-MFI (Si/Al: 40) (commercial MFI, Zeolyst CBV8014). The TOS was 10 min and the conversion and selectivity were calculated on C% molar basis. b and c) Glucose isomerization to fructose over Sn-containing zeolites: b) glucose conversion versus fructose yield and (c) reaction time versus fructose yield. The numbers in parentheses in (b) denote the Si/Sn ratios. The gray data points in (b) and (c) were obtained from previous work.[36]

formation). The rate constant for different reaction cycles was calculated assuming pseudo-first-order in glucose concentration (Figure S20). The data suggests that moderate deactivation occurs after each reaction cycle. However, the selectivity to fructose remains the same (Table S2).

Conclusion

Using a simple SDA containing moieties with conflicting effects on early crystal growth rates of MFI, we synthesized an MFI zeolite consisting of few-unit-cell crystalline domains (below ca. 10 nm) that are not crystallographically aligned. It exhibits distinct adsorption and catalytic properties from those of conventional MFI, while it shows similarities but also differences in performance when compared to SPP, another prototypical hierarchical zeolite with distinct structure. This work contributes to the quest for single-unit-cell zeolites and provides a first assessment of the adsorption and catalytic properties of few-unit-cell MFI zeolites.

Conflict of Interest

The authors declare no conflict of interest.

[1] P.-S. Lee, X. Zhang, J. A. Stoeger, A. Malek, W. Fan, S. Kumar, W. C. Yoo, S. Al Hashimi, R. L. Penn, A. Stein, M. Tsapatsis, *J. Am. Chem. Soc.* **2011**, *133*, 493–502.

[2] J. Pérez-Ramírez, C. H. Christensen, K. Egeblad, C. H. Christensen, J. C. Groen, *Chem. Soc. Rev.* **2008**, *37*, 2530–2542.

[3] M. Choi, K. Na, J. Kim, Y. Sakamoto, O. Terasaki, R. Ryoo, *Nature* **2009**, *461*, 246–249.

[4] X. Zhang, D. Liu, D. Xu, S. Asahina, K. A. Cychosz, K. V. Agrawal, Y. Al Wahedi, A. Bhan, S. Al Hashimi, O. Terasaki, M. Thommes, M. Tsapatsis, *Science* **2012**, *336*, 1684–1687.

[5] M. E. Davis, *Nature* **2002**, *417*, 813–821.

[6] A. Corma, *Chem. Rev.* **1995**, *95*, 559–614.

[7] N. Rangnekar, N. Mittal, B. Elyassi, J. Caro, M. Tsapatsis, *Chem. Soc. Rev.* **2015**, *44*, 7128–7154.

[8] M. A. Camblor, A. Corma, S. Valencia, *Microporous Mesoporous Mater.* **1998**, *25*, 59–74.

[9] L. Wei, K. Song, W. Wu, S. Holdren, G. Zhu, E. Shulman, W. Shang, H. Chen, M. R. Zachariah, D. Liu, *J. Am. Chem. Soc.* **2019**, *141*, 8712–8716.

[10] H. J. Cho, P. Dornath, W. Fan, *ACS Catal.* **2014**, *4*, 2029–2037.

[11] M. Y. Jeon, D. Kim, P. Kumar, P. S. Lee, N. Rangnekar, P. Bai, M. Shete, B. Elyassi, H. S. Lee, K. Narasimharao, S. N. Basahel, S. Al-Thabaiti, W. Xu, H. J. Cho, E. O. Fetisov, R. Thyagarajan, R. F. DeJaco, W. Fan, K. A. Mkhoyan, J. I. Siepmann, M. Tsapatsis, *Nature* **2017**, *543*, 690–694.

[12] A. Corma, M. E. Davis, *ChemPhysChem* **2004**, *5*, 304–313.

[13] S. Yang, A. Navrotsky, D. J. Wesolowski, J. A. Pople, *Chem. Mater.* **2004**, *16*, 210–219.

[14] T. M. Davis, T. O. Drews, H. Ramanan, C. He, J. Dong, H. Schnablegger, M. A. Katsoulakis, E. Kokkoli, A. V. McCormick, R. L. Penn, M. Tsapatsis, *Nat. Mater.* **2006**, *5*, 400–408.

[15] A. I. Lupulescu, J. D. Rimer, *Science* **2014**, *344*, 729–732.

[16] K. Na, C. Jo, J. Kim, K. Cho, J. Jung, Y. Seo, R. J. Messinger, B. F. Chmelka, R. Ryoo, *Science* **2011**, *333*, 328–332.

[17] C. Jo, R. Ryoo, N. Žilková, D. Vitvarová, J. Čejka, *Catal. Sci. Technol.* **2013**, *3*, 2119–2129.

[18] L. W. Beck, M. E. Davis, *Microporous Mesoporous Mater.* **1998**, *22*, 107–114.

[19] G. Bonilla, I. Díaz, M. Tsapatsis, H.-K. Jeong, Y. Lee, D. G. Vlachos, *Chem. Mater.* **2004**, *16*, 5697–5705.

[20] T. O. Drews, M. Tsapatsis, *Curr. Opin. Colloid Interface Sci.* **2005**, *10*, 233–238.

[21] S. H. Keoh, W. Chaikittisilp, K. Muraoka, R. R. Mukti, A. Shimojima, P. Kumar, M. Tsapatsis, T. Okubo, *Chem. Mater.* **2016**, *28*, 8997–9007.

[22] C. Baerlocher, L. B. McCusker, Database of Zeolite Structures: http://www.iza-structure.org/databases/. Accessed on March 29th, **2021**.

[23] C. E. A. Kirschhock, R. Ravishankar, L. V. Looveren, P. A. Jacobs, J. A. Martens, *J. Phys. Chem. B* **1999**, *103*, 4972–4978.

[24] D. D. Kragten, J. M. Fedeyko, K. R. Sawant, J. D. Rimer, D. G. Vlachos, R. F. Lobo, M. Tsapatsis, *J. Phys. Chem. B* **2003**, *107*, 10006–10016.

[25] M. A. Camblor, A. Corma, A. Mifsud, J. Pérez-Patriente, S. Valencia, *Stud. Surf. Sci. Catal.* **1997**, *105*, 341–348.

[26] Y. Guefrachi, G. Sharma, D. Xu, G. Kumar, K. P. Vinter, O. A. Abdelrahman, X. Li, S. Alhassan, P. J. Dauenhauer, A. Navrotsky, W. Zhang, M. Tsapatsis, *Angew. Chem. Int. Ed.* **2020**, *59*, 9579–9585; *Angew. Chem.* **2020**, *132*, 9666–9672.

[27] X. Zhao, S. Zeng, X. Zhang, Q. Deng, X. Li, W. Yu, K. Zhu, S. Xu, J. Liu, L. Han, *Angew. Chem. Int. Ed.* **2021**, *60*, 13959–13968; *Angew. Chem.* **2021**, *133*, 14078–14087.

[28] J. K. Reddy, K. Motokura, T. Koyama, A. Miyaji, T. Baba, *J. Catal.* **2012**, *289*, 53–61.

[29] H. Koller, R. F. Lobo, S. L. Burkett, M. E. Davis, *J. Phys. Chem.* **1995**, *99*, 12588–12596.

[30] C.-H. Cheng, D. F. Shantz, *J. Phys. Chem. B* **2005**, *109*, 19116–19125.

[31] J. S. Jeong, M. L. Odlyzko, P. Xu, B. Jalan, K. A. Mkhoyan, *Phys. Rev. B* **2016**, *93*, 165140.

[32] R. Khare, D. Millar, A. Bhan, *J. Catal.* **2015**, *321*, 23–31.

[33] R. Khare, A. Bhan, *J. Catal.* **2015**, *329*, 218–228.

[34] S. Svelle, F. Joensen, J. Nerlov, U. Olsbye, K.-P. Lillerud, S. Kolboe, M. Bjørgen, *J. Am. Chem. Soc.* **2006**, *128*, 14770–14771.

[35] L. Qi, L. Wei, L. Xu, Z. Liu, *ACS Catal.* **2015**, *5*, 3973–3982.

[36] L. Ren, Q. Guo, P. Kumar, M. Orazov, D. Xu, S. M. Alhassan, K. A. Mkhoyan, M. E. Davis, M. Tsapatsis, *Angew. Chem. Int. Ed.* **2015**, *54*, 10848–10851; *Angew. Chem.* **2015**, *127*, 10998–11001.